Journal of the Meteorological Society of Japan, Vol. 87A, pp. 223–235, 2009
DOI:10.2151/jmsj.87A.223

Two Approaches for Inter-Satellite Radiometer Calibrations between TMI and WindSat

Liang HONG, W. Linwood JONES

Central Florida Remote Sensing Laboratory, University of Central Florida, Orlando, Florida, USA

Thomas T. WILHEIT

Brazos Earth System Science, Inc., College Station, Texas, USA

and

Takis KASPARIS

Central Florida Remote Sensing Laboratory, University of Central Florida, Orlando, Florida, USA

(Manuscript received 22 June 2008, in final form 29 November 2008)

Abstract

This paper presents recent progress in inter-satellite microwave radiometric cross-calibration to eliminate brightness temperature measurement biases between a pair of radiometer channels operating at slightly different frequencies and incidence angles. The motivation of this research is to develop robust analytical cross-calibration techniques for inter-calibration of various satellite radiometer instruments, with the first projected application being the multi-satellite Global Precipitation Measurement (GPM) constellation to be launched in 2013. The significance of this work is that it will allow the formation of consistent multi-decadal time series of geophysical measurements for multiple satellite microwave radiometers that are free of instrumental biases and other long-term changes in radiometric calibration, which will allow researchers to study global climate change.

Descriptions are given for two independent calibration techniques: a Taylor series expansion of the oceanic brightness temperature (T_b) spectrum between dissimilar radiometer channels and a non-linear regression among multi-channel T_b measurements. In the first approach, predictions were made of T_b's at a destination frequency from T_b's of a close by source frequency by expansion of the oceanic brightness temperature spectrum in a Taylor series centered at the source frequency. The relationships between T_b's and frequencies were derived from simulations using a radiative transfer model (RTM), which accounts for the total collected emissions from the ocean surface and the atmosphere. Further, earth incidence angle differences between radiometer channels were transformed in a similar manner using the partial derivatives of T_b with incidence angle derived from RTM simulations. In the second approach, we used a prediction algorithm that relies on the correlation between radiometer T_b's at various frequencies and polarizations and which uses a regression on the T_b's and their non-linear transformations developed using an independent radiative transfer model.

As a demonstration, near-simultaneous pair-wise ocean T_b comparisons are presented between the TRMM Microwave Imager (TMI), which is not sun synchronous, and the sun-synchronous polar orbiting WindSat, using oceanic T_b observations from 2003-04. The corresponding results between these two inter-satellite calibration techniques are highly correlated, and results demonstrate that fixed channel-by-channel differences, of order 1 – 2 K exist between TMI and WindSat. These are significant radiometric calibration differences, which can be removed prior to forming joint data sets of geophysical parameter retrievals.

Corresponding author: W. Linwood Jones, Central Florida Remote Sensing Laboratory, University of Central Florida, Orlando, FL 32816, USA
E-mail: ljones5@cfl.rr.com

1. Introduction

The monitoring of climate is important for numerous socio-economic purposes, and satellite remote sensing provides a multi-decadal time series of geophysical parameter measurements from which climate assessments are derived. While satellites are capable of providing near-global distributions of measurements for numerical climate models, it is a major challenge to achieve sustained geophysical measurement accuracy over the lifetime of many different satellite instruments contributing to a particular data time series. Fortunately, overlapping observations of meteorological satellites provide the opportunity to maintain improved calibration accuracy, according to Goody (2002).

The motivation of this paper is to report on progress in developing robust analytical cross-calibration techniques for inter-calibration of various microwave radiometer instruments. The first application is the Global Precipitation Measurement (GPM), which relies on a constellation of cooperative satellites with a variety of microwave radiometers to make global rainfall measurements. Thus, it is crucial to achieve brightness temperature (T_b) measurement consistency at the sub-Kelvin level among the constellations, as well as to maintain sustained calibration accuracy over the lifetime of each satellite sensor. Fundamental to this concept is the existence of a core satellite in non-sun-synchronous orbit, which serves as a precipitation measurement transfer standard for the other cooperative constellation members. The issue for this radiometric comparison is that constellation satellite radiometer systems have different instrument characteristics: frequency, bandwidth, viewing geometries, calibration approaches, and antenna beam efficiencies. However, this paper presents two techniques that enable cross-calibration in spite of these instrument system differences. An example of the GPM application is presented, using the Tropical Rainfall Measuring Mission (TRMM) Microwave Imager (TMI) as a proxy for the GPM Microwave Imager, and these techniques are used to estimate the relative radiometric biases of the WindSat microwave radiometer in a sun-synchronous orbit.

The following section discusses the collocations of near-simultaneous ocean T_b's with associated relevant environmental condition "match-ups"; Section 3 describes the Taylor series expansion model and a multi-channel regression model; and Section 4 presents the inter-satellite radiometric calibration results and discusses errors.

2. Radiometers and measurement collocations

2.1 WindSat and TMI microwave radiometers

WindSat is a large-aperture, conically scanning polarimetric radiometer on the Coriolis satellite, which has a sun-synchronous orbit of 840 km altitude and 98.7° inclination. This total power radiometer operates at five frequencies (6.8, 10.7, 18.7, 23.8, and 37 GHz) with separate feed horns whose incidence angles vary from 50° to 55°, as described by Gaiser et al. (2004). Due to excellent on-orbit calibration (Jones et al. 2006; Ruff et al. 2006), we have high confidence in the T_bs from the WindSat Sensor Data Records (SDR), except during April to August when hot-load anomalies are observed near the South Pole, as noted by Twarog et al. (2006). Fortunately, this is not an issue for this paper because the TMI swath coverage exists only between ± 40° latitude, which is outside the region of this WindSat hot-load anomaly.

The TRMM conical-scanning radiometer, TMI, operates in a 350 km altitude (403 km altitude after August 2001) non-sun-synchronous orbit with a 35° inclination. TMI has five frequencies (10.65, 19.35, 21.3, 37.0, and 85.5 GHz), all at a common incidence angle of 53.2°. Post-launch radiometric calibration by Wentz, Ashcroft, and Gentemann (2001) demonstrated a systematic along-scan error of 1 K and a warm bias of 5 K caused by a slightly emissive main reflector. The TMI data products used in this paper incorporate both of these radiometric bias corrections. However, recent inter-satellite comparisons with TMI, WindSat, and SSMI reported by Gopalan et al. (2008) have revealed a small time-variable radiometric calibration error of ± 2 K, which has not been corrected in the results herein.

2.2 Measurement collocations

For meaningful T_b comparisons between a pair of satellite radiometers, it is important to have benign T_b fields; therefore, transient weather phenomena such as oceanic and atmospheric fronts and precipitation should be avoided. Furthermore, this implies that "tight" spatial and temporal collocation tolerances should exist between measurements. By analyzing T_b histograms and their statistical moments for ocean areas ("boxes") of 1° by 1° in latitude and longitude, we adopted the procedures of removing non-uniform areas and averaging T_b's over the remaining areas before comparison. Doing so reduces variability of the differences between channels.

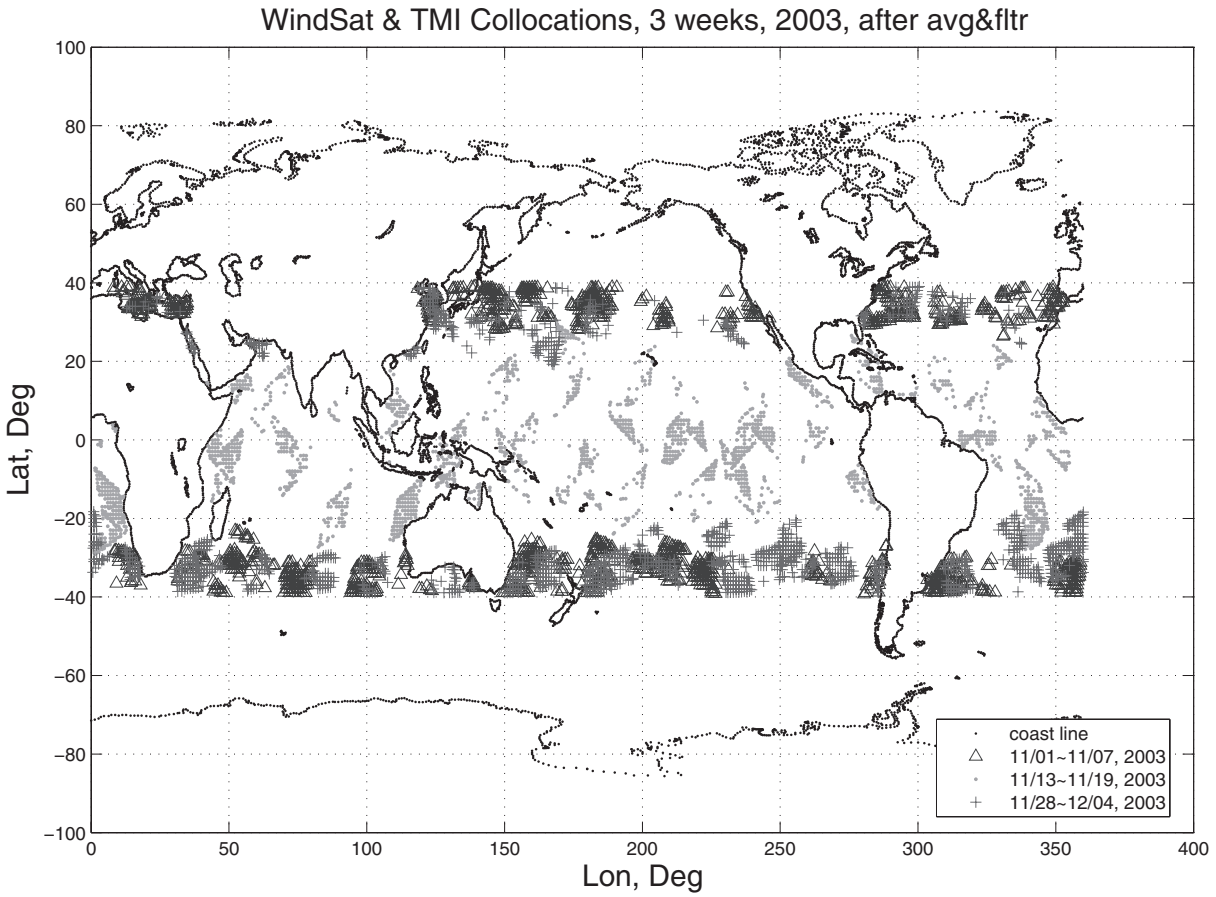

Fig. 1. Collocations between TMI and WindSat. Blue triangles denote collocations for Nov. 1-7; green dots, those for Nov. 13-19; and red crosses, those for Nov. 28-Dec. 4, 2003.

The first group of collocations between TMI and WindSat were obtained for alternating weeks during November 2003 and are mapped in Fig. 1. A second comparison dataset was chosen to examine the seasonal stability of the inter-calibration during the first week of each month between November 2003 and August 2004. Collocations during the whole month of June 2003 were collected to provide more samples for better statistical analysis. WindSat T_b's were from SDR and a total of 14,865 cases from all collocation peri-ods. The corresponding environmental parameters (sea-surface temperature (SST), ocean surface wind speed (WS), water vapor (WV), and cloud liquid water (CLW)) were from WindSat Environmental Data Records (EDR). Atmospheric profiles of temperature, pressure, and moisture were spatially interpolated to the radiometer 1° boxes using the National Oceanic and Atmospheric Administration (NOAA) National Center for Environmental Prediction's (NCEP's) Global Data Assimilation System (GDAS) atmospheric product; they were time coincident to within ± 1.5 hours. Figure 2 is an expanded view of individual T_b measurements in one collocation event (single pass). For each WindSat T_b, the geometrically closest TMI measurement (within ± 15 minutes and 25 km) was selected.

The T_b's from all TMI channels and WindSat radiometer channels were averaged over the 1° boxes. By examining the corresponding T_b means and standard deviations for each channel, we set an upper bound to screen outliers (Tables 1 and 2). The entire box was discarded if it contained only one collocated measurement, if it contained a rainy pixel, or if the standard deviation of T_b's was > 2 K for vertical polarization (V-pol) or > 3 K for horizontal polarization (H-pol). These criteria eliminated T_b outliers that had possible instrument anomalies and data that were contaminated

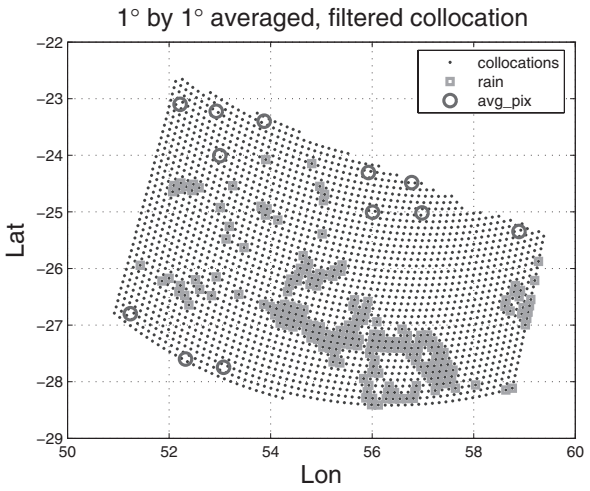

Fig. 2. Typical WindSat and TMI collocation swaths: blue dots denote individual valid collocated measurements; green squares, rain-contaminated measurements; and red crosses, valid 1° box centers.

by land or rain in the field of view.

3. Calibration approaches

Since the WindSat and TMI radiometers had similar, but not identical, frequencies and viewing angles, some translation was needed to enable comparison of collocated radiance measurements on a common basis. Fortunately, theoretical modeling of radiative transfer is well understood over the ocean and was used to provide this translation, using the following two inter-satellite calibration approaches.

3.1 Taylor series prediction

In this approach, predictions of T_b's were made at a destination (target) frequency from T_b's of a nearby source frequency by expansion of the T_b spectrum in a Taylor series centered at the source frequency. The relationships between T_b's and frequencies were derived from simulations using a radiative transfer model (RTM); earth incidence angle (EIA) differences were transformed in a similar manner, separately from the frequency adjustments.

A block diagram of this inter-satellite calibration procedure is presented in Fig. 3. Because the Taylor series expansion was calculated at the TMI incidence angle, the incidence angle transform was performed first by converting WindSat measurements to equivalent T_b's at the TMI incidence angle. Next, the source frequency with the smallest difference from the target frequency (on the same side of the WV line) was selected, and then the frequency transformations were applied. The target TMI channels and their corresponding source WindSat channels are listed in Table 3. To illustrate the magnitude of the T_b normalizations for frequency and incidence angle between the source and target channels, the delta-T_b nominal values are also listed. Of course, the actual adjustments were slightly different, based upon the collocated environmental parameters within each 1° box.

a. Radiative transfer model tuning

Since a reliable RTM is fundamental to this approach, we start with tuning and validating the model to simulate WindSat radiometer measurements. The RTM, known as RadTb, was developed by the Central Florida Remote Sensing Laboratory (CFRSL) and was based on the Environmental Modeling (ENVIMOD)

Table 1. Upper bound for WindSat T_b's over Tropical Ocean.

Channel	6.8H	6.8V	10.7H	10.7V	18.7H	18.7V	23.8H	23.8V	37H	37V
T_b (K)	120	200	150	200	200	250	230	260	200	250

Table 2. Upper bound for TMI T_b's over Tropical Ocean.

Channel	10.65H	10.65V	19.35H	19.35V	21.3V	37H	37V
T_b (K)	115	185	200	230	260	210	240

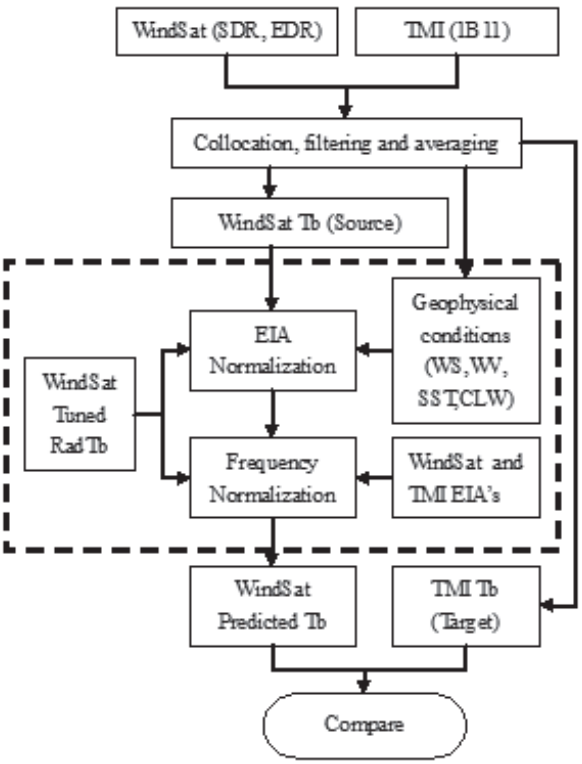

Fig. 3. Flow chart of WindSat to TMI calibration using Taylor series expansion prediction (in dash square).

model developed by Wisler and Hollinger (1977). It is driven by fourteen environmental measurements of the ocean and atmosphere, and three radiometric parameters. This RadTb version uses a sea-water dielectric constant from Meissner and Wentz (2004), a rough ocean surface emissivity formulation of Wentz and Meissner (1999), Rosenkranz's (1975, 1993) oxygen absorption model, and Stogryn's water vapor algorithm developed from Gross's formula (1955).

Prior to inter-satellite comparison, several empirical adjustments are applied to the RadTb subroutines, as described by Hong (2007), to remove T_b biases between WindSat-measured and RadTb-modeled T_bs over the range of environmental conditions experienced. The data set for tuning and validation was generated from WindSat and GDAS match-ups without rain during October 2003 (20 days).

After RTM tuning, RadTb gave excellent results between model simulations and WindSat H-pol and V-pol measurements. Very small biases were observed under the constrained training data set of environmental conditions: SST < 27°C, columnar WV < 20 mm, columnar cloud liquid < 0.1 mm, and WS < 8 m s^{-1}. For RTM validation, an expanded and independent environmental data set with 5 million cases was used, and the results are presented in Fig. 4. The overall mean biases of the RadTb simulation were < 0.5 K for the 6.8, 10.7, 18.7, and 23.8 GHz channels and < 1 K for 37 GHz. The standard deviation of the measured and modeled differences increased with frequency from 1 K at 6.8 GHz to 4 K at 37 GHz. Included in these comparisons were small systematic errors (< 1 K) associated with incorrect incidence angle corrections because the WindSat instantaneous incidence angle varied from case to case (< ± 0.5°) and the RadTb simulations were performed at fixed nominal values.

b. Frequency normalization

Under given geophysical conditions, the observed T_b is determined by the frequency and polarization of the radiometer channel, and the antenna incidence angle and azimuth angle relative to wind direction. Because the ocean wind direction relative to the radiometer azimuth look is nearly uniformly distributed over the ocean boxes, the latter effect averages to nearly 0 K.

Table 3. Source and target channels of WindSat to TMI calibration.
Example of ΔT_b under L(WS)M(WV)M(SST)L(CLW) geophysical condition, ΔT_b = TMI – WindSat.

Target: TMI f(GHz)	10.65H	10.65V	19.35H	19.35V	21.3V	37H	37V
Source: WindSat f(GHz)	10.7H	10.7V	18.7H	18.7V	18.7V	37H	37V
Freq. Norm. ΔT_b (K)	-0.10	-0.11	9.06	5.48	27.79	0.00	0.00
EIA Norm. ΔT_b (K)	-3.00	6.46	0.79	-6.79	-6.79	0.04	-0.65
Total ΔT_b (K)	-3.09	6.35	9.84	-1.31	21.00	0.04	-0.65

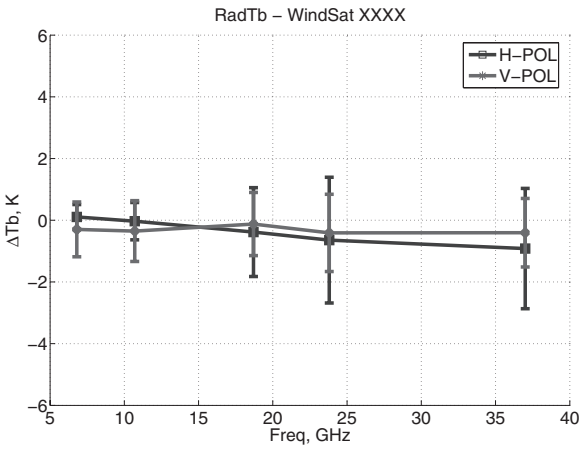

Fig. 4. RadTb validation with WindSat measurements as the reference standard under all geophysical conditions(XXXX).

Thus, by simulating satellite radiometer T_b's for specified geophysical conditions with a fixed incidence angle at V-pol and H-pol, we can derive a relationship between T_b's and operating frequency as

$$T_b = polynomial(freq), \tag{1}$$

and the Taylor series expansion $T_b(f)$ for a source f_o is

$$T_b(f_1) = T_b(f_0) + T_b'(f_0)\cdot(f_1 - f_0) + T_b''(f_0)\cdot\frac{(f_1 - f_0)^2}{2!} + T_b'''(f_0)\cdot\frac{(f_1 - f_0)^3}{3!} + T_b^{(n)}(f_0)\cdot\frac{(f_1 - f_0)^n}{n!}, \tag{2}$$

$$T_b^{(n)} = \left.\frac{\partial^{(n)} T_b(f)}{\partial f^{(n)}}\right|_{f=f_o}, \tag{3}$$

where, f_1 is the frequency of the destination channel, and f_o is the frequency of the source channel.

For the range of probable geophysical conditions, radiometer measurements were simulated for different channels from 30 days of WindSat EDRs and associated GDAS match-ups. With these geophysical parameters as inputs to RadTb, all channels of TMI and WindSat were simulated at their operating frequencies but with the incidence angle for TMI at 53.2°. Taylor series coefficients (partial derivatives) were then derived for the frequency transforms from these simulated T_b's. Frequency spectra of T_b's varied as a function of geo-physical conditions and polarization, so they were characterized separately. Of the 14 RadTb environmental inputs, only the environmental factors WS, WV, SST, and CLW were categorized. Considering the distribution of environmental conditions, the sensitivity of T_b to geophysical parameters, and the desired accuracy of frequency normalization, we categorized these four geophysical parameters into different ranges (Table 4). Thus, over 4.7 million observed environmental cases were sorted into 12,960 categories of geophysical conditions, corresponding to 6 WS × 36 WV × 10 SST × 6 CLW, which neglected the sorting of other (minor) geophysical parameters. Unrealistic conditions that rarely occur (e.g., high WV and cold SST) were eliminated so that not all of the 12,960 categories were used.

Figure 5 depicts an example of the apparent T_b spectrum, at an EIA of 53.2°, for typical environmental conditions, with the frequencies of TMI and WindSat channels identified. For cross-calibrating WindSat and TMI, Taylor series expansions were derived from similar T_b simulations with the corresponding match-up of environmental conditions.

c. Earth incidence angle normalization

Frequency and EIA transforms were performed sequentially (Fig. 3). For normalization with respect to

Table 4. Categorization of major geophysical parameters.

Classifications	Wind Speed (m/s)	Water Vapor (mm)	Sea Surface Temp. (C)	Cloud Liquid Water (mm)
Range	0 - 25	0 - 70	0 - 36	0 - 0.5
Transformation	WS/5+1	WV/2+1	SST/4+1	CLW*10+1
Num. of Levels	6	36	10	6

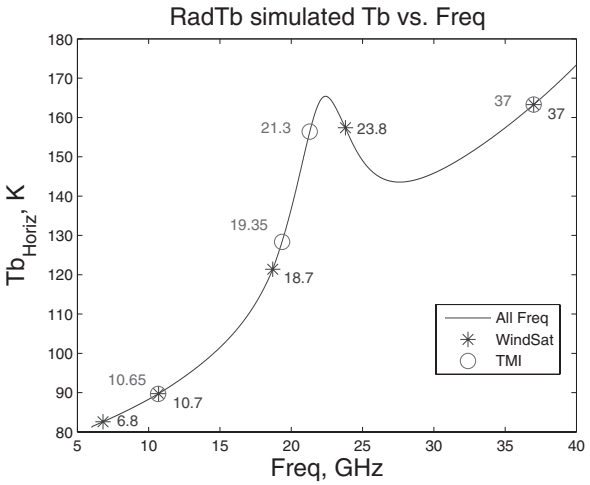

Fig. 5. Example of T_b spectrum generated from RadTb with marks at TMI and WindSat frequencies.

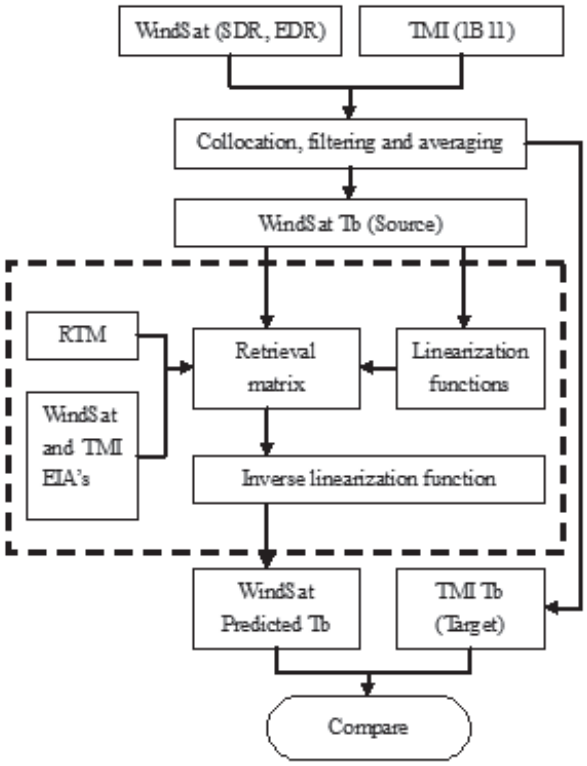

Fig. 6. Flow chart of WindSat to TMI calibration using multi-channel regression prediction (in dash square).

incidence angle, the same algorithm is applied, and the variation of T_b as a function of incidence angle is derived from the RadTb with other parameters fixed. For the full-range of environmental conditions and within the range of incidence angles of TMI and WindSat, T_b is approximately a linear function of incidence angle; thus, the transformation can be expressed as

$$Tb(\theta_1) = Tb(\theta_0) + \partial(T)/\partial(\theta) \times (\theta_1 - \theta_0), \quad (4)$$

where the partial derivative coefficients are determined for different geophysical conditions.

Because of the design of the WindSat antenna feed array, the corresponding incidence angle was different for each frequency, and the instantaneous value within each match-up box was used for the EIA transformations. From the WindSat SDRs, the lowest incidence angle was 50.4° for 10.7 GHz, and the highest was 55.9° for 18.7 GHz. For TMI, the nominal incidence angle was 53.2° (common for all channels).

3.2 Multi-channel regression calibration

This alternative approach is a slightly evolved version of the scheme used by Wilheit et al. (1984). Over oceans, the inter-satellite radiometric calibration between a pair of near-simultaneous collocated multi-channel radiometers is accomplished without requiring knowledge of the corresponding surface and atmospheric geophysical parameters. For illustrative purposes, a simplified block diagram is depicted in Fig. 6.

In this method, we use a prediction algorithm that relies on the correlation between radiometer T_b's at various frequencies and polarizations, and a regression on the T_b's (and a function of the T_b's) developed using an independent RTM (from RadTb). The logic is that GDAS models and associated radiometer environmental parameter retrievals have errors and all RTMs are imperfect; however, by using a common RTM in both the forward and the inverse sense, imperfections in the model nearly cancel out.

To simulate the training set, the starting point was the ensemble of geophysical parameters for input to the RTM. The philosophy used here was to introduce very little statistical information via the ensemble because statistically valid data sets of all of the relevant parameters were not available. Also, because we were interested in algorithms that would be robust in unusual situations, we preferred not to bias our retrievals towards commonplace situations. The ensem-

ble was chosen to exercise retrieval over the entire expected range (and perhaps more) of the relevant parameters.

Each member of the ensemble was used as input for the RTM so that radiances with the viewing parameters (angle, wavelength, polarization, noise equivalent delta-T (NEDT)) of the target instrument could be computed. It was important that the instrument noise be included in this calculation, and these viewing parameters were to be used as input to regression analysis. However, since regression is an inherently linear process and since the relationships between the radiances and the desired geophysical parameters are not close to linear, we transformed both the radiances and the desired parameters, choosing linearizing functions with knowledge of the relevant physics of the form

$$L = \ln(285 - Tb). \tag{5}$$

This function removed the bulk of the non-linearity and could be justified if we approximated the atmosphere as an isothermal layer at a temperature of 285 K. When predicting target T_b's from source T_b's, we used this form for the dependent variable and included the linear form as well for the independent variables:

$$L_{Tb\_obj} = \sum_i (c_{iL} L_{Tb\_source} + c_{iT} T_{b\_source}) + C_0. \tag{6}$$

We used a synthetic ensemble of geophysical situations to generate the T_b's of the observation (source) channels: 15 SSTs, 10 WSs, and 7 handbook atmospheres (U.S. standard, tropical, subtropical summer, subtropical winter, midlatitude summer, midlatitude winter, and subarctic summer). Also, the ensemble was designed so that the resulting retrieval would be very robust in the presence of clouds. For this reason, we included nine synthetic cloud models ranging from the null case (no cloud) up to 80 mg cm^{-2} of columnar water content. Within the cloud, the WV was increased to 100% relative humidity, and portions of the cloud colder than 233 K (the temperature of spontaneous nucleation) were assumed to be ice particles too small to have any effect on T_b's.

This combination of atmospheric and surface conditions yielded 9,450 members for the ensemble; however, to eliminate highly improbable combinations, only cases with air-sea temperature differences less than 8 K (absolute value) were included, thus reducing the number of cases to less than half of the original size. This introduced a conservative correlation between SST and columnar WV.

Regressions were then run to predict the geophysical parameters and other T_b (or linearized functions thereof) from the calculated source radiances. The matrix and offsets from this regression comprised the retrieval algorithm. As a by-product, the residuals of the regression served as an approximate performance simulation for the instrument and algorithm.

All the channels were not always needed due to a great deal of redundancy in the set of multi-channel T_b observations. Therefore, the process was iterated, deleting one channel (the one that helped least) at a time until the predicted retrieval uncertainty increased by a meaningful amount, then replacing the last channel deleted. However, when problems with the radiometer observations (e.g., radio frequency interference and instrument malfunctions) occurred, including unnecessary channels merely increased the captured cross-section for these problems. This process also enabled us to determine which linearizing function, or combination of linearizing functions, worked best.

In order to generate an algorithm for the prediction of the TMI T_b's from that of the WindSat, we generated a database using the above ensemble, which included all of the TMI and WindSat channels as well as the logarithmic forms for each. The values of the SST, WS, WV, and CLW were included, as well as a few channels that did not actually exist (e.g., TMI 21.3 GHz H-pol) but maintained symmetry, for ease of programming. Reasonable noise estimates were included for all the independent variables but not for the dependent variables. In total, the database consisted of 32 variables, and the covariance matrix of these data was used as the input for the regression analysis.

This formalism permitted a test of self-consistency of the T_b's, and the T_b of one channel of a given instrument could be predicted from the remaining channels. In this case, we predicted the 19.35 GHz (18.7 GHz) channel of TMI (WindSat) from the remaining channels. Using the April and July 2003 data sets (WindSat IDR and TMI 1B11 v5), the mean bias (Predicted-Observed) for these channels was 1.25 K (0.31 K) for April and 1.06 K (-0.62 K) for July. These results suggested that WindSat was somewhat better calibrated than TMI and, more importantly, gave us confidence in the self-consistency of the method.

4. Results and discussion

4.1 WindSat to TMI calibration

First, three groups of collocations between WindSat and TMI were analyzed during November 2003. In

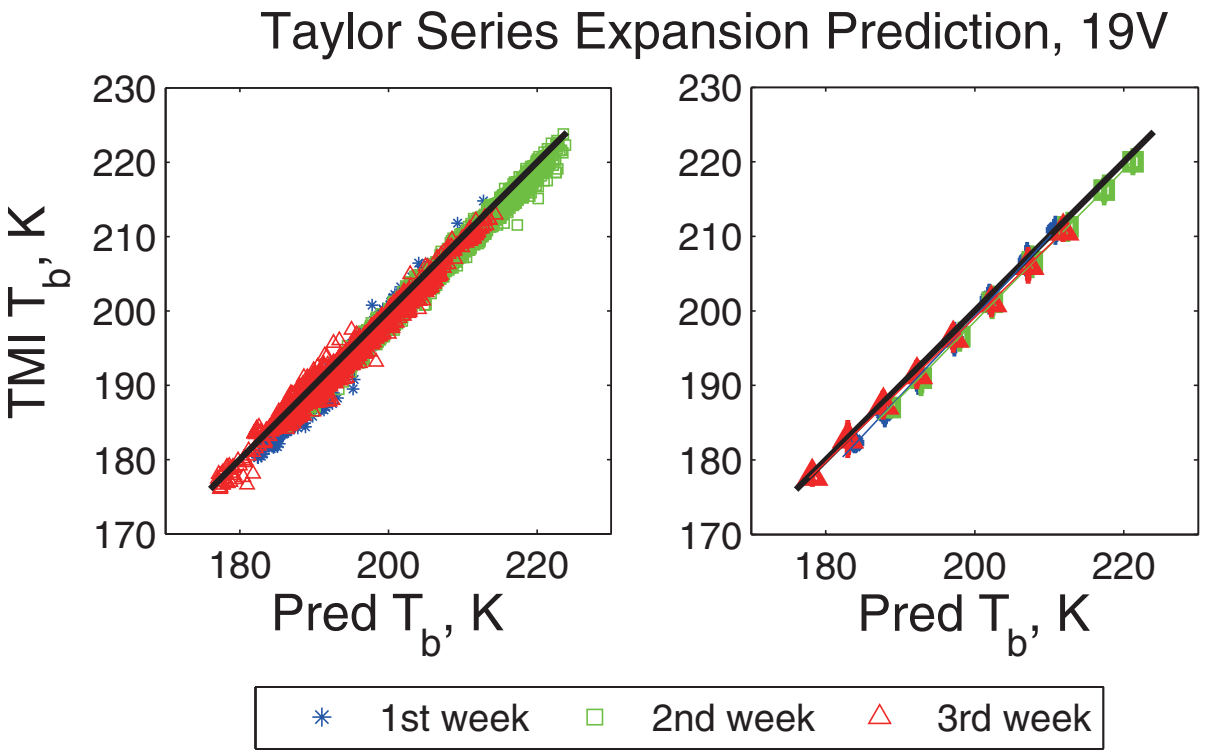

Taylor series expansion, TMI = Slope * Pred + Offset:

Linear fit coefficients	1st week	2nd week	3rd week
Slope	1.07	1.02	0.97
Offset	-13.99	-4.99	5.09

Fig. 7. Example of TMI-WindSat T_b comparisons for the TMI 19.4 GHz V-pol using the Taylor Series Expansion method. The left panel is a scatter diagram with collocated measurements for three weeks in Nov. 2003, and the right panel is the linear regression by week.

over 1000 cases in each week-long period, T_b's were binned to 1° boxes and average values were calculated for each box, excluding rainy and noisy data where the standard deviation exceeded a fixed threshold.

A typical example of the comparison between the WindSat-predicted and the TMI T_b for the 19V channel is presented in Figs. 7 (Taylor series) and 8 (multi-channel regression). These figures present all data for the three periods: blue for the first week, green for the second week, and red for the third week. The T_b's for the first and third weeks overlap at the low end of the T_b scale, and the second week covers the higher values. The reason can be seen in Fig. 1, where the collocations for these three periods are grouped by latitude. The collocations for the second week are distributed within ± 20° latitude, whereas those for the first and third weeks have absolute latitudes > 20°. The linear regression fits by the weekly data sets (the right-hand panels of both figures) indicate similar results for both methods but slightly different biases (offsets).

The statistics of mean differences between predictions from WindSat channels and TMI observations by Taylor series expansion are indicated in Table 5, and similar results from multi-channel regression are presented in Table 6. A few channels exhibit excellent agreement: for example, the 10.65 H-pol and the 37 H-pol results differ by 0.2 K, as do the 21 V-pol for the first and third weeks. However, for most channels, the two methods yield significant fixed differences (1 to 1.7 K) between biases. A closer examination of the

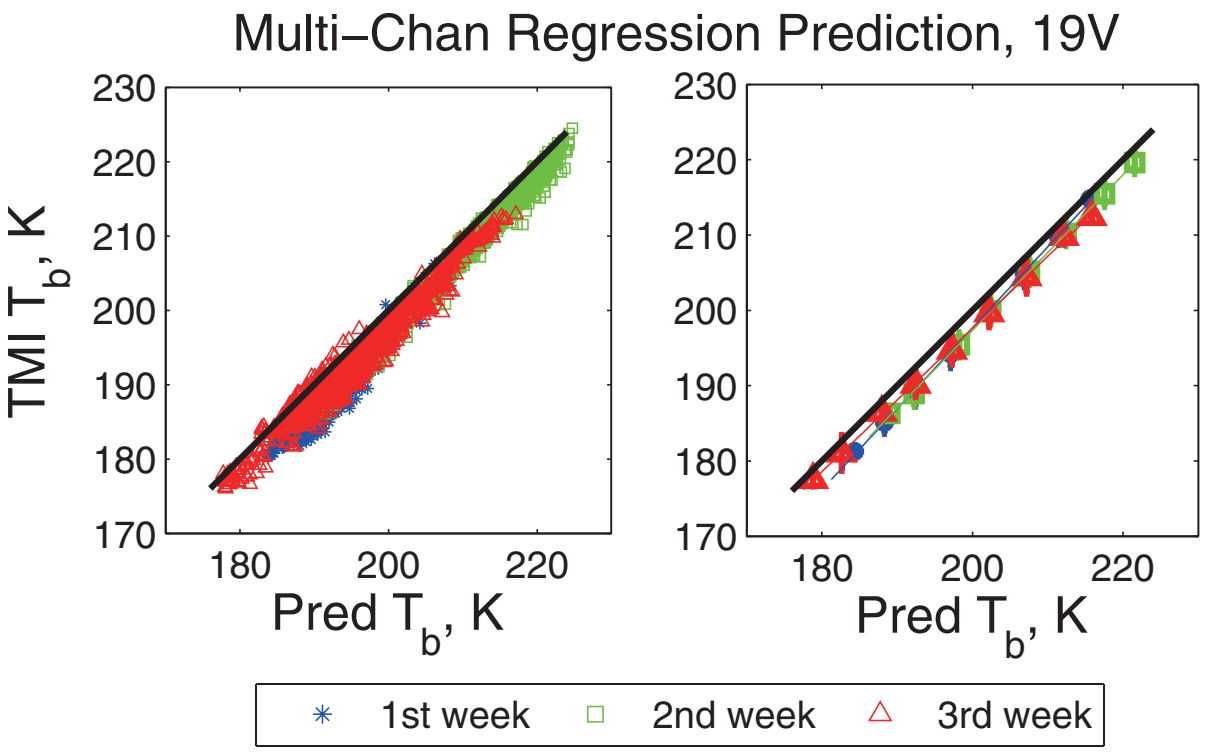

Multi-channel regression, TMI = Slope * Pred + Offset:

Linear fit coefficients	1st week	2nd week	3rd week
Slope	1.07	1.03	0.95
Offset	-17.31	-9.35	6.90

Fig. 8. Example of TMI-WindSat T_b comparisons for the TMI 19.4 GHz V-pol using the multi-channel regression method. The left panel is a scatter diagram with collocated measurements for three weeks in Nov. 2003, and the right panel is the linear regression by week.

week-to-week changes reveals a very high correlation between channels (once constant offsets are removed), which is encouraging. For example, the differences between the corresponding weekly sets of channel biases exhibit a systematic decrease over the one-month time span of 0.8 K in all channels, which suggests a possible short-term drift of calibration in one or both radiometers. This hypothesis of time-varying radiometric calibration has been confirmed by Gopalan et al. (2008), who identified a ± 2 K systematic variation in the TMI radiometric calibration. This is consistent with the week-to-week results of both calibration methods here.

Another group of WindSat and TMI collocated data were analyzed by selecting one week's collocations per season from November 2003 to August 2004. Results from both calibration approaches reveal biases between predictions and measurements similar to those in Tables 5 and 6 from the November group. The seasonal fluctuations of T_b biases are within a smaller range of 0.5 K. According to the sparse sampling of this year-long period, no seasonal drift was found for the cross-calibration between WindSat and TMI. For all the collocations (14,865 cases) between WindSat and TMI (Table 7), the standard deviations of the biases between predictions and measurements are at the same level (1 K) for both approaches, and no pattern of ΔT_b as a function of geo-location or geophysical conditions is found in our analysis. For both approaches, the biases for most channels are greater

Table 5. ΔT_b in WindSat to TMI prediction by Taylor series expansion (3 weeks data).

Δ= Prediction -TMI		10H	10V	19H	19V	21V	37H	37V	# cases
11/01-11/07	mean	2.32	0.09	4.34	1.26	3.50	2.87	3.26	1311
11/13-11/19	mean	1.92	-0.32	4.04	1.19	5.21	2.38	3.17	1983
11/28-12/04	mean	1.51	-0.78	3.50	0.58	2.69	1.77	2.37	1522
Total 3 Weeks	mean	1.88	-0.36	3.95	0.99	3.91	2.32	2.94	4816
	std	0.89	0.86	1.02	0.98	1.75	1.22	1.04	

Table 6. ΔT_b in WindSat to TMI prediction by multi-channel regression (3 weeks data).

Δ= Prediction -TMI		10H	10V	19H	19V	21V	37H	37V	# cases
11/01-11/07	mean	2.10	1.47	2.63	2.67	3.61	2.63	4.29	1311
11/13-11/19	mean	1.79	1.20	2.48	2.29	3.13	2.58	4.30	1983
11/28-12/04	mean	1.21	0.86	1.87	1.80	2.76	1.62	3.52	1522
Total 3 Weeks	mean	1.71	1.14	2.31	2.27	3.14	2.34	4.02	4816
	std	0.94	0.82	1.10	1.07	1.25	1.23	1.25	

than the 1 to 2 K absolute calibration accuracy specified by the radiometer developers; however, Table 7 is in general agreement with the results of Gopalan et al. (2008).

4.2 Radiometric inter-calibration error analysis

The inter-satellite calibration biases are a combination of actual sensor calibration differences and errors associated with the comparison methodology. The major error sources that were considered in establishing the cross-calibration accuracy are discussed in the following paragraphs. Despite some unknowns, our conservative estimate for the overall random error is of the order < 1 K for both techniques.

a. Errors common to both techniques

Two major errors are common to both prediction techniques. First is the T_b measurement precision or NEDT. This zero-mean Gaussian random error is reduced to a negligible value (<< 0.1 K) by the square root of the number of T_b observations averaged within a 1° box.

The second error is associated with simultaneous and collocated T_b observations. The antenna's instantaneous fields-of-view will never be exactly the same, nor will the times of observation; thus, some random

Table 7. ΔT_b in WindSat to TMI prediction by two approaches for all cases 14,865 cases in total.

Δ= Prediction -TMI		10H	10V	19H	19V	21V	37H	37V
Taylor Series	mean	1.93	-0.26	4.09	1.11	4.65	2.58	3.02
Expansion	std	0.78	0.80	0.85	0.88	1.71	1.07	0.88
Multi-Channel	mean	1.78	1.18	2.59	2.30	3.18	2.69	4.14
Regression	std	0.84	0.84	0.93	0.91	1.12	1.08	1.10

error will always exist in matching the scenes of apparent T_b's that vary both temporally and spatially with existing geophysical conditions. However, our temporal and spatial tolerances for collocations between WindSat and TMI are strict enough to prevent significant changes in geophysical conditions that could cause large variations in T_b. Thus, the binned averaging and filtering over relatively large 1° boxes and the removal of large random outliers mitigate these issues. Furthermore, the large number of collocations yielded Gaussian statistics and a random error estimate of < ± 0.3 K (Hong 2007).

b. Errors associated with Taylor series

Translation to a common frequency and incidence angle basis results in residual error since it uses an imperfect RTM and regression curve fitting to produce the Taylor series coefficients. Furthermore, these normal-izations depend on the actual oceanic and atmospheric environmental conditions, which are estimated from available satellite retrievals and NOAA GDAS numerical weather models to provide the necessary RadTb environmental inputs. The resulting frequency interpolation errors were estimated from the modeling residuals to be ± 0.2 K to ± 0.7 K for frequencies between 10 GHz and 37 GHz, except near the WV channel, which is ± 1.25 K (Hong 2007).

Also, according to RadTb model simulations, T_b varies linearly with the TMI incidence angle of 53.2°. In the frequency range of 5 to 40 GHz, the vertically polarized T_b varies with the incidence angle with a slope of 2 to 2.5 K/deg; however, the horizontally polarized T_b's are less sensitive with a slope of - 1 K/deg for frequencies under 10 GHz, and within ± 0.5 K/deg for frequencies between 10 and 40 GHz. In the 1° boxes where the T_b comparisons are made, the average incidence angle is used to make the EIA adjustment, and the uncertainty of this angle is < 0.1° one sigma. Thus, for the WindSat channels, the T_b random error introduced by the knowledge of EIA is less than ± 0.25 K for V-pol and ± 0.1 K for H-pol.

Finally, the ocean surface emissivity anisotropy is determined by the relative wind direction (difference between the radiometer antenna azimuth line of sight and the wind direction); failure to account for this introduces a small error of the order a few Kelvin. Since the ocean emissivity anisotropy is zero mean when averaged over all directions and since the two satellites in any collocation never have the same viewing direction, the relative wind direction is approximately uniformly distributed, and the effect on T_b averages to zero. However, the differential between collocated measurements is a known error of unknown magnitude, and this remains a task for future analysis.

Combining these independent sources of error, the overall estimated rms error is less than 1 K.

c. Errors associated with multi-channel regression

The multi-channel regression method relies upon the correlation of T_b between all radiometer channels. The covariance matrix correlations are estimates of the "true correlations" that are derived using an imperfect RTM, which results in errors. Further errors in the source channel T_b's produce errors in the derived biases, although this technique is less susceptible to single-channel errors than the Taylor series technique. Finally, the RTM used for multi-channel regression training was different than the RadTb used for the Taylor series approach. Thus, differences between these two techniques could be partially attributed to the RTMs used. Our error estimate for this technique, based upon the residuals of the self-consistency for WindSat testing described above, is ± 0.6 K.

5. Conclusion

In this paper, we performed cross-calibrations on a sun-synchronous polar orbiting satellite microwave radiometer, WindSat, using the non-sun-synchronous radiometer TMI as a calibration transfer standard (and a proxy for the future GPM Microwave Imager). These multi-channel microwave radiometers were cross-calibrated using near-simultaneous, pair-wise comparisons of T_b measurements over rain-free tropical ocean areas after applying the Taylor series prediction and the multi-channel regression T_b normalization procedures. The significance of this paper is in the presentation of these inter-satellite radiometer calibration techniques rather than the quantitative determination of the biases between WindSat and TMI.

The Taylor series prediction approach has critical dependence on the radiometric calibration quality of a single nearby source frequency channel (Taylor expansion center frequency) and a reasonable estimate of the corresponding environmental condition match-ups. This approach applies universally to the calibration of any radiometer channel pair, and once the Taylor series coefficients are produced, the RTM is no longer needed in cross-calibration for different radiometer pairs. This approach transfers the source radiometric calibration and enables cascaded linear calibrations with other polar orbiting radiometers that do not overlap in time.

However, the multi-channel regression prediction

approach has the advantages that it removes dependency on collocated geophysical match-ups, and it spreads the dependency on multiple-frequency channels. Therefore, a single degraded source channel does not seriously affect the calibration result.

This paper presents radiometric biases between TMI and WindSat derived using these independent approaches. The corresponding results are highly correlated between techniques, and the fixed channel-by-channel differences of magnitude 1 to 1.5 K are within the estimated error bounds. Furthermore, the Satellite Radiometric Cross-Calibration (X-CAL) Working Group of the National Aeronautics and Space Administration's (NASA's) Precipitation Measurement Missions Science Team is currently evaluating a number of techniques (including the Taylor series and multi-channel regression described in this paper) and will eventually arrive at a consensus approach to be applied for the level-1C T_b calibration algorithms for the GPM.

Acknowledgments

This work is sponsored by NASA Goddard Space Flight Center TRMM Project. The authors would also like to thank Mr. James Johnson for the helpful comments and valuable discussions.

References

Gaiser, P. W., K. M. St. Germain, E. M. Twarog, G. A. Poe, W. Purdy, D. Richardson, W. Grossman, W. L. Jones, D. Spencer, G. Golba, J. Cleveland, L. Choy, R. M. Bevilacqua, and P. S. Chang, 2004: The WindSat spaceborne polarimetric microwave radiometer: sensor description and early orbit performance. *IEEE Trans. Geosci. Remote Sens.*, **42**, 11, 2347–2361.

Goody, R., J. Anderson, T. Karl, R. B. Miller, G. North, J. Simpson, G. Stephens, and W. Washington, 2002: Why monitor the climate? *Bull. Amer. Meteor. Soc.*, **83**, 873–878.

Gopalan, K., W. L. Jones, T. Kasparis, and T. Wilheit, 2008: Inter-satellite radiometer calibration of WindSat, TMI and SSMI, *Proceedings of IEEE IGARSS 2008*, Boston, MA, USA., July 6-11.

Gross, E. P., 1955: Shape of collision-broadened spectral lines. *Phys. Rev.*, **97**, 395–403.

Hong, L., 2007: Inter-satellite microwave radiometer calibration. Doctoral dissertation, University of Central Florida.

Jones, W. L., J. D. Park, S. Soisuvarn, L. Hong, P. W. Gaiser, and K. M. St. Germain, 2006: Deep-space calibration of the WindSat radiometer. *Geoscience and Remote Sensing, IEEE Transactions on*, **44**, 3, 476–495.

Meissner, T., and F. J. Wentz, 2004: The complex dielectric constant of pure and sea water from microwave satellite observations. *IEEE TGARS*, **42**(9), 1836–1849.

Rosenkranz, P. W., 1975: Shape of the 5mm oxygen band in the atmosphere. *IEEE Trans. AP*, **AP-23**, 4, 498–506.

Rosenkranz, P. W., 1993: Absorption of microwaves by atmospheric gases. *Remote Sensing by Microwave Radiometry*, M. A. Janssen, Ed., John Wiley & Sons, New York, Chapter 2.

Ruf, C. S., H. Ying, and S. T. Brown, 2006: Calibration of WindSat polarimetric channels with a vicarious cold reference. *IEEE Trans. Geosci. Remote Sens.*, **44**, 3, 470–475.

Thompson, S. D., 2002: Evaluation of a microwave radiative transfer model for calculating satellite brightness temperature. Master's thesis, University of Central Florida.

Twarog, E. M., W. E. Purdy, P. W. Gaiser, K. H. Cheung, and B. E. Kelm, 2006: WindSat on-orbit warm load calibration. *IEEE Trans. Geosci. Remote Sens.*, **44**, 3, 476–495.

Wentz, F. J., 1997: A well-calibrated ocean algorithm for SSM/I. *J. Geophy. Res.,* **102**, 8703–8718.

Wentz, F. J., and T. Meissner, 1999: AMSR ocean algorithm, version 2. Remote Sensing Systems, Santa Rosa, CA, *RSS Tech. Rep.* 21599A.

Wentz, F. J., P. Ashcroft, and C. Gentemann, 2001: Post-launch calibration of the TRMM microwave imager. *Geoscience and Remote Sensing, IEEE Transactions on*, **39**, 2, 415–422.

Wilheit, T. T., Jr., J. R. Greaves, J. A. Gatlin, D. Han, B. M. Krupp, A. S. Milman, and E. S. Chang, 1984: Retrieval of ocean surface parameters from the scanning multifrequency microwave radiometer (SMMR) on the Nimbus-7 satellite. *Trans IEEE Geosci. Remote Sens.*, **GE-22**, 2, 133–143.

Wisler, M. M., and J. P. Hollinger, 1977: Estimation of marine environmental parameters using microwave radiometric remote sensing systems. *NRL Memo Rpt 3661*, Nov., Naval Research Laboratory, Wash DC, 7-86.